

PAPER • OPEN ACCESS

## High frequency copolymer ultrasonic transducer array of size-effective elements

To cite this article: Adit Decharat *et al* 2018 *Smart Mater. Struct.* **27** 025001

View the [article online](#) for updates and enhancements.

### Related content

- [Effect of polymer electrode thickness on the acoustical properties of all-screen printed piezoelectric PVDF copolymer transducers](#)  
Adit Decharat, Sanat Wagle and Frank Melandsø
- [Evaluation of adhesive-free crossed-electrode poly\(vinylidene fluoride\) copolymer array transducers for high frequency imaging](#)  
Sanat Wagle, Adit Decharat, Anowarul Habib et al.
- [Ultrasonic measurements of surface defects on flexible circuits using high-frequency focused polymer transducers](#)  
Sanat Wagle, Anowarul Habib and Frank Melandsø

# High frequency copolymer ultrasonic transducer array of size-effective elements

Adit Decharat<sup>1</sup>, Sanat Wagle, Anowarul Habib, Svein Jacobsen and Frank Melandsø<sup>1</sup>

Department of Physics and Technology, UiT The Arctic University of Norway, Tromsø, Norway

E-mail: [adit.decharat@uit.no](mailto:adit.decharat@uit.no) and [frank.melandso@uit.no](mailto:frank.melandso@uit.no)

Received 29 May 2017, revised 21 September 2017

Accepted for publication 6 October 2017

Published 5 January 2018



CrossMark

## Abstract

A layer-by-layer deposition method for producing dual-layer ultrasonic transducers from piezoelectric copolymers has been developed. The method uses a combination of customized and standard processing to obtain 2D array transducers with electrical connection of the individual elements routed directly to the rear of the substrate. A numerical model was implemented to study basic parameters effecting the transducer characteristics. Key elements of the array were characterized and evaluated, demonstrating its viability of 2D imaging. Signal reproducibility of the prototype array was studied by characterizing the variations of the center frequency ( $\approx 42$  MHz) and bandwidth ( $\approx 25$  MHz) of the acoustic. Object identification was also tested and parameterized by acoustic-field beamwidth as well as proper scan step size. Simple tests to illustrate a benefit of multi-element scan on lowering the inspection time were conducted. Structural imaging of the test structure underneath multi-layered wave media (glass plate and distilled water) was also performed. The prototype presented in this work is an important step towards realizing an inexpensive, compact array of individually operated copolymer transducers that can serve in a fast/volumetric high frequency (HF) ultrasonic scanning platform.

Keywords: copolymer-based transducer, multi element scanning, P(VDF-TrFe), multi layer transducer, high-frequency piezoelectric transducer, high frequency ultrasonic imaging

(Some figures may appear in colour only in the online journal)

## 1. Introduction

Ultrasonic scanning systems using high-frequency (HF) copolymer piezoelectric transducers have attracted considerable interest for sensing and imaging in both non-invasive industrial and biological applications [1–4]. PVDF and its copolymers have both disadvantages and advantages with respect to PZT for producing transducers. In addition to the flexibility and chemical resistance already mentioned, PVDF benefits from its low acoustic impedance which makes coupling to e.g. water and polymer materials much easier for broad

band applications. When it comes to disadvantages, PVDF for example, has much lower piezoelectric coupling coefficients than PZT. It also has a higher temperature sensitivity, higher material losses, and obtain a material depolarization at lower temperatures. On the other hand, the weaker piezoelectric coupling in combination with much higher loss (both dielectric and elastic) make it possible to apply unpatterned films for HF transducers. This will simplify the production process significantly compared to PZT, where typically the ceramic layers have to be processed into a composite structure using e.g. a diamond cutting blade or a laser. The increased complexity from producing composite PZT in dual layers for HF application is probably the largest advantages for using PVDF or other piezo materials that can be used as a non-patterned layer. Other advantages with PVDF is the ability of using several low-thermal processing methods, e.g. [5–7], making the material an attractive component for low-end transducer and sensor production where, typically, manufacturing simplifications are

<sup>1</sup> Author to whom any correspondence should be addressed.



Original content from this work may be used under the terms of the [Creative Commons Attribution 3.0 licence](https://creativecommons.org/licenses/by/3.0/). Any further distribution of this work must maintain attribution to the author(s) and the title of the work, journal citation and DOI.

important issues. In addition, the mechanical flexibility allows the material film to be curved on to the specimen surface as well as withstand a high mechanical stress. Polymers are therefore often a material of preference in flexible electronic/harsh vibrated area sensor/actuators [8].

Electronic-based scan array with a large number of active transducer elements are now frequently used in both medical and industrial applications. The array structure offers a number of benefits, e.g. in terms of tunable beam and focus increasing processing speed on parallel platforms. However, there are many challenges involved in manufacturing the arrays for HF applications. These are typically associated with the elaborate micromachining process for producing the transducer to meet the physical requirements of the array configuration (e.g. for aperture areas, element-to-element pitches and material thicknesses), and individual electrical connection of a large number of elements [9–13]. It also becomes increasingly complicated from a production point of view, to avoid severe cross-talk between transducer elements as the frequency increases. Mechanical scanning of a single element can therefore be an acceptable option for some applications, for example in HF ultrasonic microscope systems [14]. Nevertheless, a single-element scanning system undergoes a huge drawback; increased inspection time. As a likely solution, based on the number of operating elements, mechanical scanning of multi-single elements has potential to improve performance of a single-element-based scanning system. In the design consideration for HF multi-element transducer platform, one often has to consider tradeoffs between costs, sensitivity and data acquisition time. Other factors like the effective platform dimension and weight may also be important since they can influence the sweep rate of the scanning platform motor [15]. Thus, an instrumentation equipped with a number of single commercial transducers (e.g. piston [16]) would be disqualifying for such a purpose.

In the current manuscript, we will focus on transducers made from the copolymer between poly(vinylidene fluoride) and trifluoroethylene (PVDF-TrFE). Our aim has been to build prototypes of dual-layer copolymer transducers on a constrained substrate area containing a number of active elements, and to explore a solution for an efficiently electric-signal connection. Unlike previous works where electrode connection lines are typically brought out horizontally to the edge of the array (see for example [17]), and with adopted concept from electronic 3D integration, we have implemented a method for producing via connectors allowing individual element connection directly from the backside of the transducer. This method will typically produce a shorter and more uniform signal path lengths for the transducer elements, which again will have benefits in terms of delay times and parasitic capacitance, resistance and inductance [18]. These improved characteristics also allow simplifications in array signal calibration as well as electronic network design. The proposed connection method is realized from well-established etching and deposition methods, which potentially can be scaled-up to a large number of elements. For our dual-layer transducer prototypes, it has also been a goal to avoid adhesives in the assemble process to obtain benefits with respect to

sensitivity [17, 19–21]. A number of tests were also done on the prototypes, including, pulser-receiver characterization, probe scanning of emitted sound fields, and imaging tests. A part of the investigation has been to demonstrate how multi-element acquisition and mechanical scanning can be combined to reduce the overall imaging time. Tests to illustrate the advantage of a multi-element scan over the traditional single-element method on lowering the inspection time were also conducted.

## 2. Transducer elementary design and assembling consideration

The proposed transducer design uses a layer-by-layer approach to build up the required materials on top of a polymer substrate. This substrate will also act as the transducer backing. It has been a goal to obtain a scalable method in which size, number of transducer elements and layers could be varied. Basically, we wanted to establish reliable methods for individual electrical connection for a multi-layer transducer array design. In the current work the proposed design is implemented on a dual-layer transducer involving two polymer-piezoelectric layer and three electrode layers.

For operating the thickness-mode dual-layer transducer with polymer backing and water load [22] at frequencies around 40 MHz, each single piezo-polymer layer was assigned to be 12  $\mu\text{m}$ . To allow a numbers of HF transducer element in 2D array, proper design and assembly of the electrode and its connection should be carefully considered. One possibility is to connect all electrode layers directly to the backside for each element. As for multilayer copolymer actuators, methods that have been reported for inter-layer signal connection are stepwise-hole fabrications. To access the embedded electrodes inside the polymer layer, the polymers are stepwise removed by plasma etching [23] and laser cutting [24]. Nevertheless, these methods involve complicated equipment and processes which influence product throughput may be inapplicable for low-end transducer production. Drilling through the substrate by mechanical means can provide fast processing holes with acceptable finish-hole size required for our application.

In the current work, a mechanical drill tool was used to drill through the composite material layer at the signal line location close to active area. The opening also enable cross-sectional access of the drilled embedded electrodes inside the composited-polymer layers. Importantly, residual from drilling process inside the hole (e.g. drill lubricant oil, polymeric burrs forming at a drilled embed-electrode interface) may result in defective interconnection causing failure in transducer poling. Thus, careful cleaning is needed. Besides that, to gain either vertical mechanical or electrical inter-layer connection robustness of a relatively thin electrode layer sandwiched by (i.e. soft) polymer layers, the electrode layer should be made thicker. However, in HF ultrasonic transducers, thick electrode layers have shown to influence transducer properties [25]. Additional processes have been added to locally fabricate the thick metallic pad at the electrode-arm

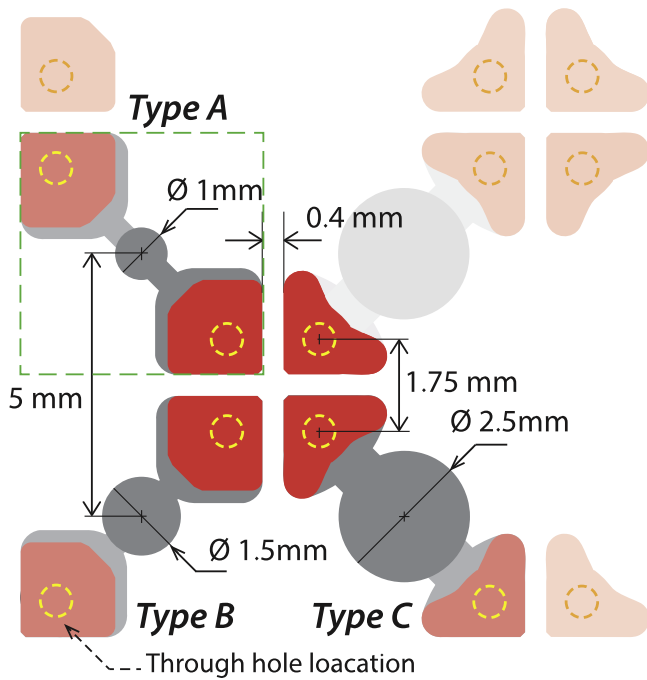


**Figure 1.** Example of the top-view configuration used for the array elements and their arrangement with the pitch of 5 mm. Here red color illustrates the thick metal pad areas and gray colors the thin electrode layer areas (intensive colors are used for the upper electrode layer).

end (where via-hole interconnecting take place), while the active area is maintained as thin as possible.

It should be noticed that our 2D design unlike tunable beam-arrays previously mentioned, is based on operating the individual elements as single transducers since there is a very small overlap between the individual ultrasonic beams. This means that beam steering is not an issue for our array design, as for many other array applications. Therefore, the design layout has no rigorously constrains on dimensions, as for instance for linear arrays [10], and will in general, be defined by the application and the available assembling platform.

The number of deployed array elements  $N$  (or element per unit area) is one of the important parameters in fast volumetric inspection where the acquisition time can be expedited approximately by a factor of  $N$ . In the presented study, the  $8 \times 8$  effective pixel elements were designed to accommodate into the  $4 \times 4 \text{ cm}^2$  substrate area. To yield a better directional beam [26] and higher emitted power for the apertures, the diameter  $D$  must be significantly larger than the longitudinal operation wavelength  $\lambda$ . Thus, a transducer design where  $D \gg \lambda$ , will be of our interest. This constrain combined with the desired requirement for resolution (when applied for C-scan imaging) which on the other hand, is inversely proportional to  $D$ , are used to define the aperture. Based on previous-mentioned criteria, a number of three different aperture designs; 1 mm (denoted as type A), 1.5 mm (type B), and 2.5 mm (type C), were made and placed together in same array, to establish the same batch process condition for a future comparative study. In addition, all element designs were assigned to have the same pixel size and pitch

which the drawing of the top-view layout of each element type and the element arrangement are depicted as in figure 1. The element pixels are here electrically isolated by a gap of 0.4 mm.

### 3. Dual-layer array prototyping

In this work we use high performance polyethylenimine (PEI) as a backing substrate with the product name Ultem<sup>1</sup>. This polymer substrate with thickness around  $850 \mu\text{m}$  provides good thermal stability (for our processing temperatures  $\leq 135^\circ\text{C}$ ) and good impedance matching to the copolymer layer. Also, its low acoustic attenuation allows us to estimate important transducer properties, which will be discussed later.

#### 3.1. Adhesive-free layer assembling

A layer-by-layer process-step flow for making the transducer array is illustrated in figure 2 where the principle fabricating processes of the layer shown in the right side and a detail of additional processes for electrode/pad layer shown on the left. Transducer assembly initially starts with a plasma treatment of PEI substrate to improve surface bonding as in right (a) step of figure 2. Then a 60 nm thick silver (Ag) layer was deposited on one side of the substrate using a sputter coater (Cressington 208 h). This Ag layer acts as a seed layer for a copper layer that in the following step was electroplated to a nominal thickness around  $3 \mu\text{m}$  (left (a) step of figure 2). After deposition, the two metallic layers were patterned by an in-house printed circuit board (PCB) photolithography platform using a transparent foil mask to pattern photoresist layer, and then selectively chemical etching to produce thick conductive pads that later will be for via connections as the steps shown in left (b) and (c) of figure 2. After patterning the pad, a much thinner electrode was produced in areas containing the active circular shaped apertures and connecting arms to these (hereafter we will refer to these thin metal layers as the active areas). This was done by sputtering an Ag-layer over the whole substrate to a thickness of around 80 nm, followed by photolithography patterning (left (d) and (e) of figure 2). Then selectively etching a silver layer that completed the first electrode pattern sitting on the substrate as shown in (f). In the next step, as in right (c) step of figure 2, a P(VDF-TrFE) copolymer (molar ratio 77:23), Piezo Tech (Arkema Group)<sup>2</sup> solution was deposited by spin coating. After spinning, wait a couple minutes to let spun liquid settle a level, and then degassed the sample in 1 mbar vacuum atmosphere to vaporize the solvent which leave the dried layer to a final thickness around  $12 \mu\text{m}$ . The sample was then annealed at  $135^\circ\text{C}$  for more than 4 h to eliminate residual solvent, and particularly, enhance the  $\beta$ -phase crystallinity. Sufficient anneal temperature and period will also allow the copolymer film to withstand our successive chemical process (e.g. acetone). Thereafter, as in right (d) step of figure 2, the second

<sup>1</sup> [www.sabic.com](http://www.sabic.com).

<sup>2</sup> [www.piezotech.eu](http://www.piezotech.eu).

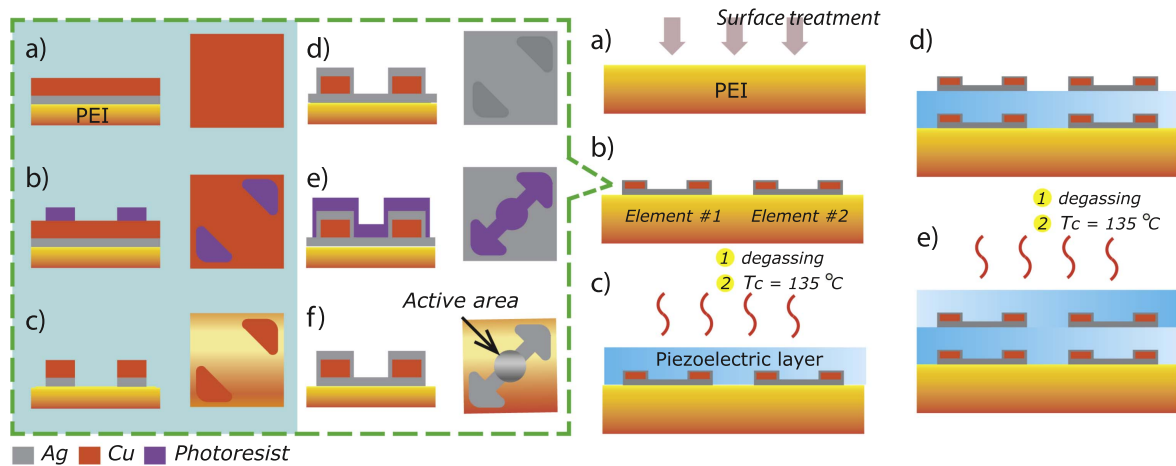


**Figure 2.** The adhesive-free layer-by-layer process shown in incorrect proportions for illustration purposes. This includes principle deposition process steps for making transducer layers (right side), and the process steps for implementing electrode layers with additive thick-metallic pads (left side). The aside images show a top view of each step.

electrode layer (previously aligned to the first electrode structure) sitting on top of the first P(VDF-TrFE) layer, was produced using the previous described steps (figure 2, left), yielding both thin Ag-electrodes in the active areas, and much thicker Ag/Cu pads used for via connections. By repeating the previous described steps, the second P(VDF-TrFE) layer was deposited right (e) of figure 2, and finally a third electrode layer was added which completed the layer-by-layer assembly method.

### 3.2. Through-hole connection

A sample  $8 \times 8$  element array of dual-layer copolymer elements is shown in figure 3(a). For this sample the via pads for the individual transducer elements were thoroughly drilled using a computer numerical control machine to produce holes with 0.8 mm diameter (see figure 1 for drilling distance in the cluster). Before epoxy filling, the through holes were prepared by, firstly, at the transducer front side, using a small-tip diamond bit to grind inside the drilled hole with relatively-slow rotation while submerging in acetone bath. After that the sample was rinsed by isopropanol solvent prior to cleaning with soap water. A high pressure from tap water was created to thoroughly clean inside the hole before rinsing with distilled water. The sample was blown by a nitrogen blower to remove the liquid from the transducer active area side, then treated with heat at  $110^\circ\text{C}$  for 30 min to eliminate the moisture. Using a needle tip, dipping into the substance, to convey small amount of epoxy into a tiny hole toward from both sides, each hole was filled up with conductive epoxy to produce connecting vias between the electrode planes were needed. It should be noted that this method could be made more efficient in the future using conductive-past printing as described in [5] or [27]. Small conductive pins were prepared for further connection of electrodes to the electronics. To obtain a reliable and fast assembly method for a large number of pins, a jig was prepared containing all pins at spatial positions corresponding to the via hole locations. After epoxy filling, all pins were slowly inserted into the holes (with

uncured paste inside) by splicing the array substrate to the jig from the top. Whilst inserting the pins, the substrate was shaken to help the epoxy spread uniformly inside the holes.

The spliced substrate was curing at  $80^\circ\text{C}$  in the oven overnight. After conductive-epoxy curing, the jig was removed leaving only the pins attached to the substrate. The electric connections of all electrode layers were enabled and directly brought out to the backside of the substrate as shown in figure 3(b), making it very easy to provide electrical connection to the individual transducer elements. Undesired electrical contact among the pins in the cluster, caused by overflowed epoxy, were checked and removed by blade if needed. At the front side, extended pins/pads were covered by silicone adhesive to improve electrically HF isolation of different opposite poles while operating in the water.

## 4. Characterization, modeling and evaluation

Before the array transducers could be characterized using ultrasonic transceiver electronics, the transducer elements were poled by the method described in [5]. Initially 15 transducer elements were poled as three sets of different aperture diameters, containing five elements each.

### 4.1. Transducer frequency-dependent characteristics

The experiments in this section were focused on the reliability test of the purpose-built transducers by the reproducibility of the characteristics, and then compared to simulation results. For simplification and to eliminate a possible effect caused by a fluid-test setup, characterizing was based on piezoelectric layers and the backing without any significant element loading (only surrounding air). In a first test of our prototype, the signal reproducibility among the poled array elements was investigated via frequency-response characteristic. Transducer and the characterizing equipment that consists of programmable arbitrary-wave generator (Agilent, 81150A), a current amplifier (FEMTO, DHPA-100) and digital

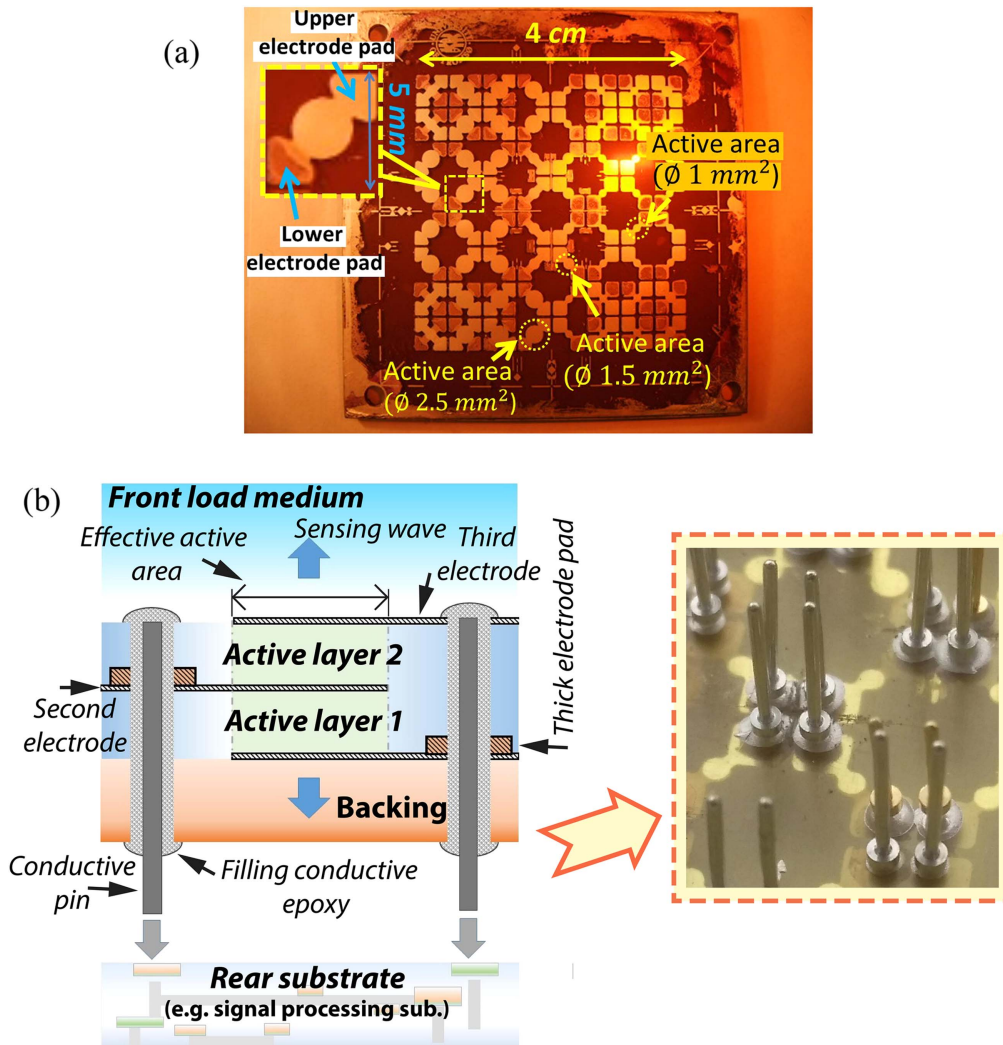


**Figure 3.** (a) Optical image showing a front view of the transducer array, and inserted image viewing a magnification of a transducer element. (b) A cross-sectional diagram illustrating an individual dual-layer transducer element is shown in the left figure while the right figure yields a zoomed optical image of the substrate’s backside including mounted pins.

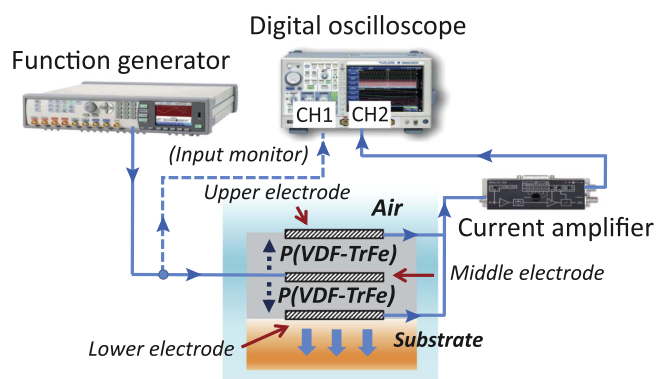


**Figure 4.** Instruments and connection paths used for the frequency response characterization. The transducer is operated as a transceiver.

oscilloscope (Yokogawa, DLM 6054), are connected together as detailed in figure 4. The transducer electrode i.e. at the middle is connected to the signal generator while the upper/lower electrode are connected together and brought out to the current amplifier (polarity direction indicated by dash-line

arrow in the layer). The element was driven by an ultra-wideband pulse given by the 2nd derivative of a Gaussian pulse. This pulse which is also known as the Ricker wavelet or the Mexican hat distribution, can be expressed as

$$v(t) = V_0 \exp(1 - 2\pi^2 f_M^2 t^2) \exp(-\pi^2 f_M^2 t^2), \quad (1)$$

where  $V_0$  is the pulse amplitude, and  $f_M$  is a frequency parameter where the amplitude spectrum maximizes in the frequency space. For the experimental investigation  $f_M = 30$  MHz was used, producing a broadband spectrum that covers well the frequency band obtained for the transducer response. The transducer elements were driven in air without any coupling fluid in front, yielding a strong back-propagating wave through the PEI backing substrate. Since the substrate is quite thin with a relative small acoustic attenuation, the ultrasonic reflection initiated from substrate backside could easily be observed and used further to estimate for example, frequency responses and uniformity among elements of the same size. To achieve this, the acoustic reflection generated from the total current received on the upper and lower

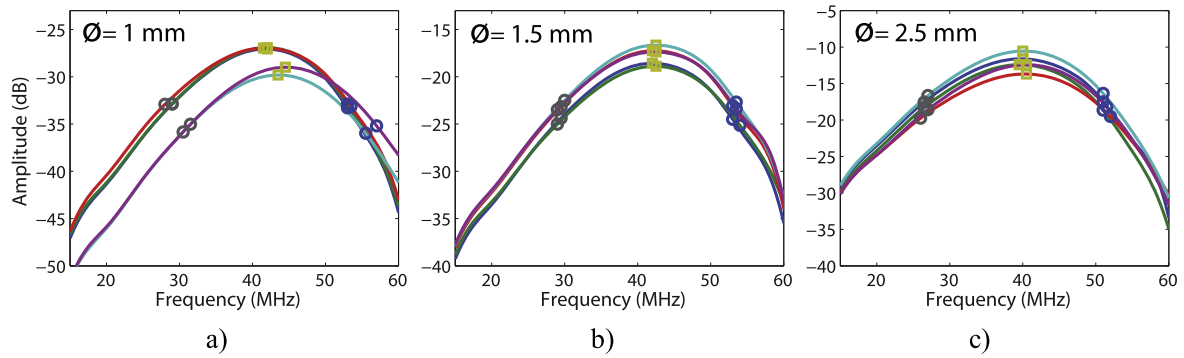


**Figure 5.** Experimental frequency responses for the three transducer types (a) type A (1 mm), (b) type B (1.5 mm), and (c) type C (2.5 mm) after normalizing the measured amplitude spectra with the input spectrum for the driver pulse. Each figure contains responses from five transducer elements.

**Table 1.** Frequency statistics for the different transducer types with data calculated from 5 elements for each type.

Transducer type	Average center freq. (MHz)	Center freq. standard deviation (MHz)	Percent difference from average center freq. (%)	Average 6 dB bandwidth (MHz)	Bandwidth standard deviation (MHz)	Percent difference from average bandwidth (%)
Ø 1.0 mm	42.7	1.25	2.9	24.8	0.76	3
Ø 1.5 mm	42.3	0.27	0.6	24	0.7	2.9
Ø 2.5 mm	40.1	0.42	1	24.7	0.76	3.1

electrodes, was magnified by the current amplifier, and loaded into oscilloscope channel 2. The reflected signal was processed further on the oscilloscope by first isolating the reflection from the PEI-air interface using an appropriate time window, and then converting the time gated signal to the frequency domain using the built-in Fourier transformation function. The potential used to drive the transducer was also measured on the oscilloscope and loaded into channel 1, processed into amplitude spectrum, and stored as a text file together with the amplitude spectrum for the reflection (channel 2). The stored spectral information in a dB-scale, was then processed further by MATLAB to obtain frequency response for the received current (channel 2) normalized with respect to the driving pulse (channel 1). Since all stored spectral information are in a dB-scale, this normalization can be done quite easily by just subtracting the driving amplitude spectrum from the reflection spectrum, yielding the frequency responses shown in figure 5 for the various aperture types (A, B and C as previously described) and transducer elements (five for each aperture type). For each aperture type we have also listed statistical parameters in table 1 for the obtained central frequencies and bandwidths. The results show a signal average center frequency and 6 dB bandwidth for all apertures to be 41.7 MHz and 24.5 MHz, respectively. Electrical characteristics were also measured using an LCR analyzer (Agilent, E4982A). Similar to the pulse measurements, the transducers were characterized with air as the surrounding medium. These measurements taken at 40 MHz, gave 1446  $\Omega$ , 450  $\Omega$  and 168  $\Omega$  for the mean value of real part of the impedance for apertures A, B, and C, respectively. The corresponding imaginary parts were measured to 2.97, 9.12 and 30.0 pF when expressed as capacitive values.

#### 4.2. Numerical modeling

A finite element model (FEM) was also implemented in COMSOL Multiphysics to simulate the dual-layer transducer system. The simulation was based on COMSOL's axisymmetric 2D model with material properties and dimensions corresponding to a type A aperture with diameter 1.0 mm. This aperture was implemented by the geometry shown in figure 6(a) with a radial dimension equal to half the aperture size. A default symmetric boundary condition was used on the left-side boundary, while constraints were implemented on the right boundary for the displacement and electric field to allow only 1D longitudinal wave motion. This approach combined with an asymmetric rectangular computational grid, made it possible to compute solution at only a small fraction of time compared to a full 2D simulation. At the same time the constrained FEM, which is expected to give results similar to a KLM model, will cover the dominant wave features generated by the longitudinal mode. The lower part of the computational domain includes the PEI backing with thickness 0.85 mm used in the transducer prototypes, mass density 1270 kg m<sup>-3</sup> (specified for the used Ultem 1000 material), and longitudinal phase velocity 2460 m s<sup>-1</sup> (estimated from previous experiments), yielding 3.1 MRayl for the PEI acoustic impedance. For the upper and lower boundaries, a free-moving boundary condition was used on the elastic material to model reflection from air which has an impedance much lower than the used polymers.

In order to model the experimental characterization closely, the FEM model was solved in the time domain with the transducer excited by a Ricker wavelet given by equation (1), with a amplitude  $V_0 = 1$  and  $f_M = 30$  MHz. This pulse and

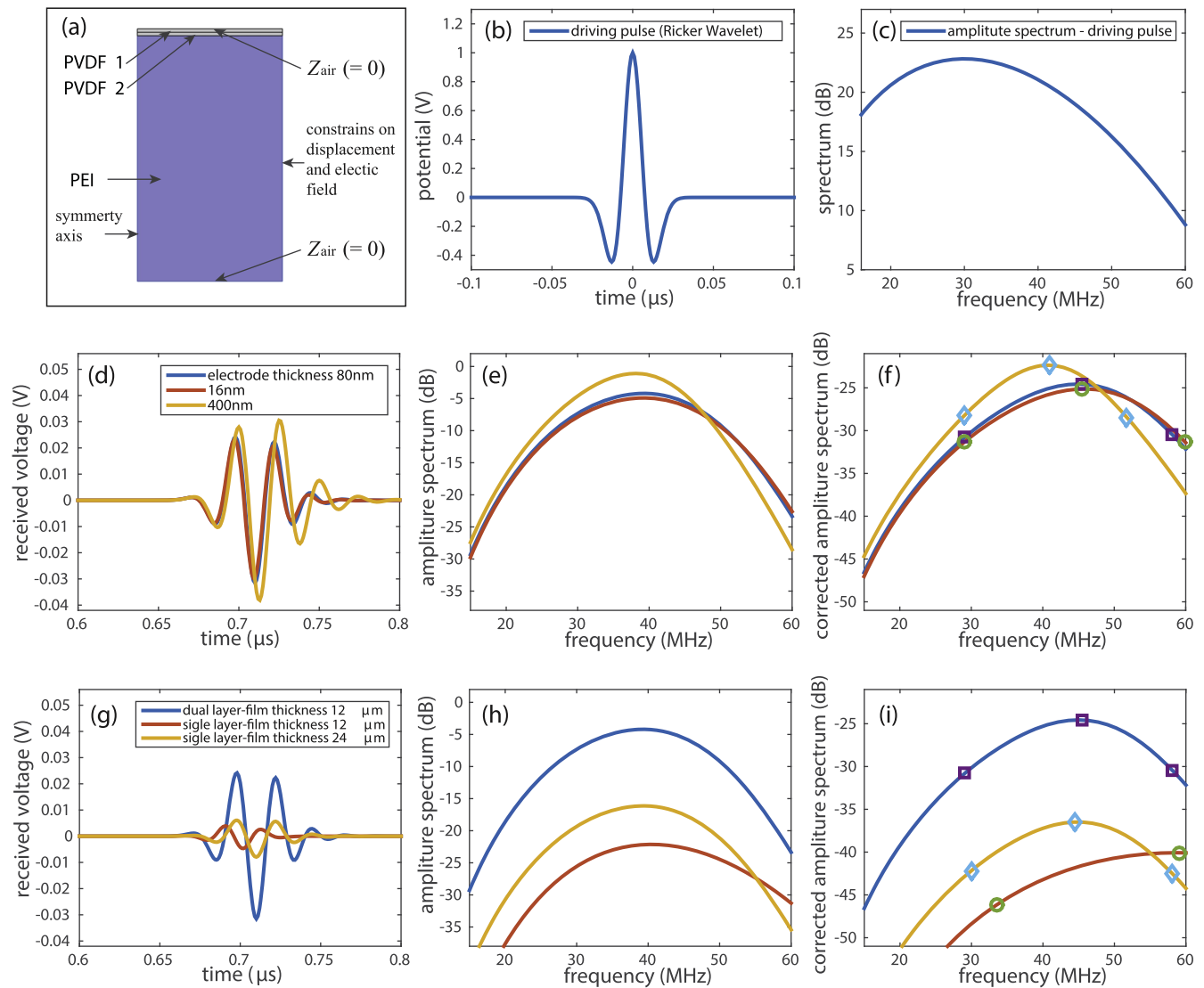


**Figure 6.** Figure panel showing the FEM simulation results and (a) the computation domain including information about applied materials and boundary conditions. The driving pulse (input signal) is shown both in (b) time and (c) frequency domain. The middle figures show the acoustic response signals from three different thickness electrodes ( $D_{16nm}$ ,  $D_{80nm}$ , and  $D_{400nm}$ ) both in (d) time and (e) frequency domain as an amplitude spectra. These spectra were also normalized with respect to the input spectrum shown in (c), to obtain (f) the simulated transducer response with center frequency and  $-6$  dB bandwidth limits indicated by the symbols. In the lower figures the dual-layer configuration used in our prototypes ( $D_{80nm}$ ) has been compared to single layer transducers with P(VDF-TrFE) thicknesses 12 and 24  $\mu m$  ( $S_{12\mu m}$  and  $S_{24\mu m}$ ). These figures show (g) the time responses with (h) corresponding spectra, and (i) the transducer frequency response after normalizing with the input spectrum.

its amplitude spectrum are shown in figures 6(b) and (c), respectively. One should notice that although the amplitude here is not the same as the one used for the experimental characterization, it should be possible to compare the experimental and numerical amplitude spectra after normalizing with respect to the amplitude spectrum of the excitation pulse.

For the first part of the numerical investigation we wanted to explore how the electrode thickness would influence the frequency response. The electrode thickness 80 nm  $D_{80nm}$  used in the transducer prototypes for electrodes in the active domains, were therefore compared to a much thinner  $D_{16nm}$  (16 nm) and thicker  $D_{400nm}$  (400 nm) electrodes, with reflected pulses in the time domain shown in figure 6(d). The corresponding amplitude spectra are shown in figure 6(e), and

after normalizing with the driving spectrum in figure (f). For the latter figure, the frequencies giving the highest response (used as the center frequencies), and the frequencies given a  $-6$  dB attenuation on both sides, are all indicated by spot symbols. Numerical values for the center frequencies,  $-6$  dB bandwidth, and  $-6$  dB bandwidth in percentage of the center frequency, are also listed in table 2. From figure 6(f) and table 2, we notice a relative small change in the frequency response as the electrode thickness is reduced from 80 nm (used in the prototypes) to 16 nm. This suggest that the used 80 nm electrode thickness for the sputtered silver electrodes, will only give a minor reduction in the transducer center frequency and bandwidth. However, the numerical findings for a 400 nm thick electrode e.g. yielding a significant

**Table 2.** Obtained center frequencies and bandwidths from the numerical study.

Transducer	Center frequency (MHz)	Bandwidth (MHz)	% Bandwidth (MHz)
$D_{16\text{ nm}}$	45	31	68
$D_{80\text{ nm}}$	45	29	64
$D_{400\text{ nm}}$	41	23	56
$S_{12\mu\text{m}}$	59	52	88
$S_{24\mu\text{m}}$	45	28	63

reduction in the bandwidth, points out that the electrode thickness is a critical parameter that should be kept as low as possible.

We also wanted to compare the performance obtained from a dual-layer transducer, with similar single-layer transducers. Two single layer transducer with P(VDF-TrFE) film thicknesses  $12\ \mu\text{m}$  ( $S_{12\mu\text{m}}$ ) and  $24\ \mu\text{m}$  ( $S_{24\mu\text{m}}$ ) were therefore simulated under the same conditions as for the dual-layer transducer, with the obtained reflections from the PEI-air interface shown in figure 6(g). The spectra and normalized spectra to these reflections are shown in figure (h) and (i), respectively. As expected, we notice a significant reduction in the signal amplitude as the number of layers are reduced from two to one, e.g. with differences in peak values in the frequency domains which are of the order of the theoretical gain factor 4. We also see that the thinnest single layer transducer yields a much higher central frequency and bandwidth than the other two, while these parameters are comparable for the other two transducers. These findings suggest that it is mainly the total transducer thickness (including all layers) that determines the shape of the frequency response, and that a significant increase in the amplitude can be obtained using a dual-layer construction.

#### 4.3. Acoustic field distribution

To evaluate the ultrasonic field radiated by the transducer, a needle hydrophone was scanned in a two-dimensional plane (hereafter defined as the  $xy$ -plane) parallel to the substrate plane. By repeating the  $xy$ -plane scan for different hydrophone-transducer distances ( $d$ ), it was possible to gain a 3D view of the pressure field distribution around each transducer element. To perform automated measurements we used a water tank scanning system provided by Precision Acoustics Ltd<sup>3</sup> (Dorchester, UK) containing dual-channel programmable arbitrary-wave generator (Tektronix, AFG 3102), hydrophone, amplifiers, scanning actuators and software.

As a wave transmitter, the element was excited by the Gaussian-modulated sinusoidal burst where the pulse mathematically expressed as

$$v(t) = \exp\left[-\frac{(t-t_0)^2}{2\sigma_o^2}\right] \sin[2\pi f_o(t)], \quad (2)$$

where,  $t_0$  is time delay,  $\sigma_o$  is Gaussian pulse width and  $f_o$  is

frequency of sinusoidal component. Fundamental waveform was programed separately prior to uploading to the function generator. During the operation test, the frequency and number of cycles in a burst were turned to yield a center frequency around 40 MHz for the acoustic response received in water. In the experiment, as shown in figure 7, a traveling acoustic wave is generated from the transducer, which receives its signal from a 50 W rf-amplifier with bandwidth from 250 kHz to 150 MHz (Electronics and Innovation 350 L). Due to the damage-voltage limitation of the amplifier input port ( $\leq 1V_{\text{rms}}$ ), a 20 dB attenuation block was used for overdriving protection on the input signal excited by signal generator. The near-field regions for transducer types A, B and C at a center frequency of 40 MHz (with  $37\ \mu\text{m}$  as the estimated wavelength in water), were estimated to 6 mm, 15 mm and 42 mm, respectively. Data acquisition was performed by scanning the  $75\ \mu\text{m}$  diameter hydrophone probe (receiver) over a square area in the  $xy$  plane. The probe was initially moved over the aperture front (with the center of scan area aligned to the aperture center), with all parts submerged in a sufficiently deep bath of distilled water (see also inset image in figure 7). The resulting pressure magnitude data (in arbitrary units) is shown in figure 8. Here the left figures in the  $3 \times 2$  figure panel show the acoustic pressure distributions in  $xy$ -plane at the distances given in the figures. These distances were either approximately at, or just beyond, the near-field region. On the right side of figure 8, the pressure profiles along the  $x$ -axis are shown at three different  $d$ -values given in the figure captions. Information about the  $-6$  and  $-12$  dB beamwidths are also provided in the figures.

The smallest  $-6$  dB beamwidth, of a size around the aperture half width, occurred at a distance that is slightly beyond the near-field region. To perform a scanning, the beamwidth was initially taking into consideration. An approximation of the  $-6$  dB beamwidth ( $w$ ) at a distance  $L$  from the transducer surface, can be determined by  $w = 2L \tan(\theta/2)$ , where  $(\theta/2)$  is  $-6$  dB half-beam spread angle. In the remote field this angle is given by

$$\sin\left(\frac{\theta}{2}\right)_{-6\text{dB}} = \frac{0.704 V}{2 r f}, \quad (3)$$

where  $V$  is the sound velocity in test media ( $1496\ \text{m s}^{-1}$  for distilled water at  $25\ ^\circ\text{C}$ ),  $r$  is radius of the transducer element and  $f$  is transducer operation frequency. For  $f = 40$  MHz, this yields the  $-6$  dB beam width of different  $L$  as shown in figure 8 (in parenthesis below measurement data). It is also interesting to observe that the pressure field distributions of all considered samples show a high degree of symmetry.

#### 4.4. Structural imaging

The ability of using the transducer prototypes for C-scan imaging application was also explored. This was done using transducer elements of type A or B connected only to a current amplifier (FEMTO DHPA-100). In the following sections, the transducer will be operated in transceiver module (similar to transceiver module in figure 4 but with wave coupling at the front). More details regarding the

<sup>3</sup> [www.acoustics.co.uk](http://www.acoustics.co.uk).

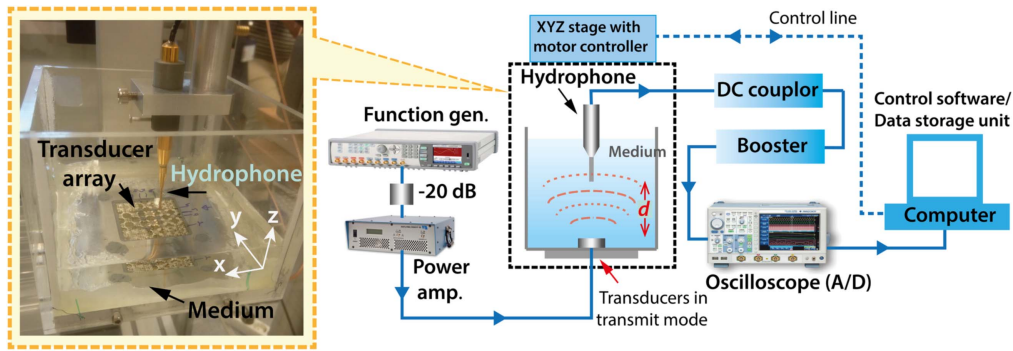


**Figure 7.** Instruments and experiment setup used to measure the acoustic radiation field by hydrophone scanning. The inset image shown the used water tank with a transducer prototype and hydrophone inserted.

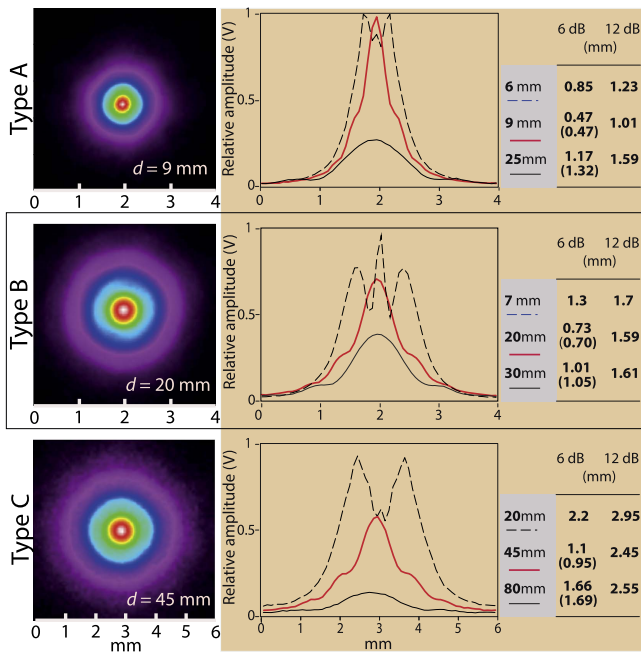


**Figure 8.** The measured relative pressure-field distributions for the three transducer types. Here the left figures show the front-view field pattern at distance slightly beyond the near-field region, while the right figures display profile-view field patterns. The profiles are measured at different distances  $d$  with beam width estimates and calculated 6 dB beamwidths given inside the brackets.

experimental setup and used instruments are shown in figure 9. From a drawing, the transducer system can be operated in two different modes which are stand-alone and two-element operation mode. The element was excited directly from a source to generate a sensing pulse wave while moving along the  $xy$  plane under a test specimen. Scanning waves reflected by the specimen were detected with the same element prior to amplifying by a current amplifier which was set to  $10^4 \text{ V A}^{-1}$  gain, yielding a 80 MHz bandwidth. Similar pulse function and burst control parameters as in section 4.3 are used. It should be noted that to maximize a signal-to-noise ratio of HF system, having a short transmission line from sensing element to the first-stage amplifier is essential. To display the results, digitally-storage data of 2D scan signal were processed in MATLAB to create a C-scan image by employing a match-filter signal detection algorithm. Such

technique, for which the process algorithm illustrated in figure 10, are frequently used in radar and sonar applications to improve the signal-to-noise ratio of the received signal. As an example, the multi-received echoes from a single scan position is shown in figure 11(a). A specified time-window of this signal covering the features of interest, is taken out and showed in figure 11(b) together with the specified signal shape (template) used for the match filter. Here the right and left side figures show these signals in the time and frequency domains, respectively. The time window and the match filter are then convoluted, yielding the signal shown in figure 11(c). From this convolution, we then can extract the maximum signal amplitude ( $I_{\max}$ ) which is used as the pixel intensity for the generated images.

To obtain an adequate spatial-resolution for an image, the scan distances  $d$  for each of the element types were slightly beyond the near field distance estimated in figure 8. Figure 12(a) shows an optical image of a standard PCB with a one side copper pattern that will be used as a test object for our imaging. The test board with thickness 1.6 mm contains 2D structures (circles and rectangles) with different sizes, made from etching the plated Cu with thickness  $30 \mu\text{m}$ .

Initially, we wanted to investigate the influence of the spatial step size used for the scanning, and imaged the PCB board first with a coarse scan step  $300 \mu\text{m}$  with a stand-alone type A element transducer. This gave the amplitude image shown in figure 12(b) for scanning a  $12 \times 15 \text{ mm}^2$  area at a distance  $d = 10 \text{ mm}$ . In figure 12(c) this imaging was repeated, but with a finer scan step of  $75 \mu\text{m}$ . By comparing the ultrasonic image figures 12(b) and (c) with the optical one in figure 12(a), we notice that both images are capable of displaying most of the fine details in the etched copper. However, some of the finest structures shown in the copper areas of figure 12(c) are not visible in figure 12(b), and the latter image is also more influenced by discrete pixel effects. One should notice that the  $300 \mu\text{m}$  step sizes used in figure 12(b) is quite close to the expected beam resolution, e.g. estimated to  $470 \mu\text{m}$  at  $d = 9 \text{ mm}$  in figure 8. It is therefore likely that the image in figure 12(b), to some degree, suffers from spatial under-sampling. Below the images, we also plotted the values along a horizontal line going through the smallest circle indicated with the left arrow in figure 12(c).

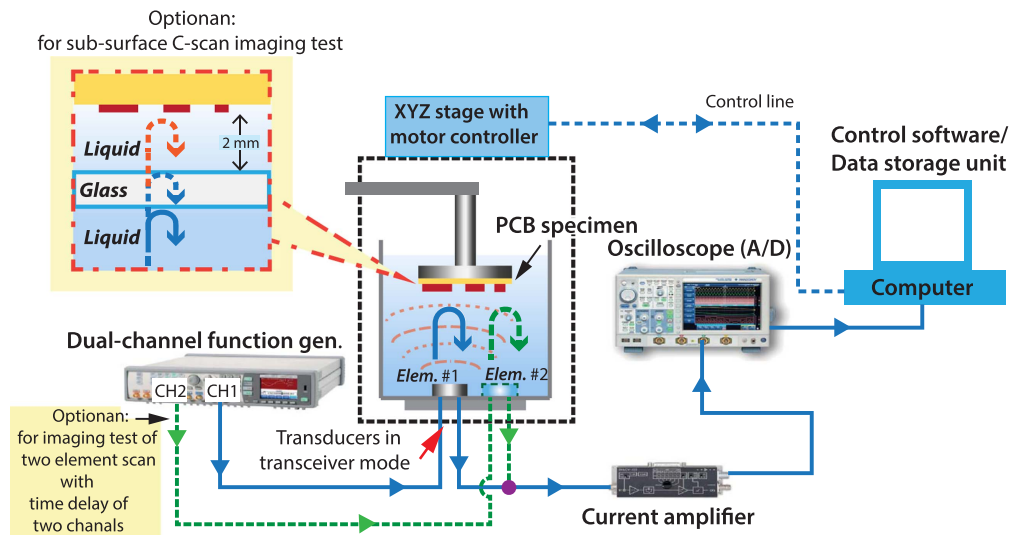


**Figure 9.** Schematic drawing of the instrumentation and signal-flow line used for the C-scan imaging experiment; for stand-alone element operation mode (solid-blue line) and for optional two-element operation mode (solid-blue together with green-dash line). The inset drawing shows cross-section view of the specimen with front obstacle layer (glass plate) with 2 mm gap, forming multi-layered wave medium. Also, basically echo-wave mechanism caused by discontinuously acoustic impedance of the composited materials are depicted.

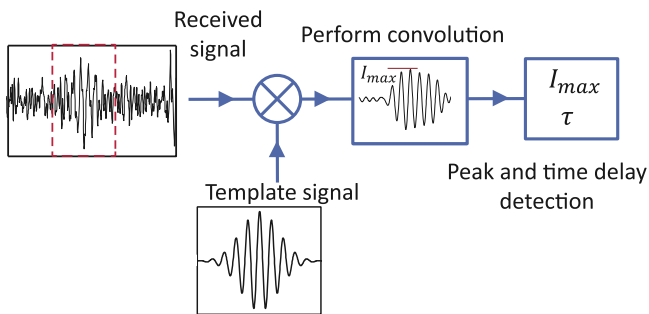


**Figure 10.** Schematic flow diagram used for the match filter signal detection. A time window of the received signal and the template are convolved in time yielding correlated amplitude versus time delay data. Then the system detects the maximum value and its time delay.

Next we wanted to compare the image quality obtained by different aperture sizes, and repeated the fine step scanning ( $75 \mu\text{m}$ ) with aperture B instead of A. For the resulting images shown in figure 12(d), the separation distance  $d$  was increased to 20 mm to avoid near field effects. From the image we see that the smallest structures, indicated with the arrows in figure 12(c), are also visible in figure 12(d), but more smeared out than in figure 12(c). The under-laying line plot also shows that all intensity transitions at the copper edges are more smeared out giving a more blurred image. We believe that the increased blurring (or reduced image resolution) is mainly is due to the increased beamwidth for aperture B, e.g. estimated to  $730 \mu\text{m}$  for a  $-6 \text{ dB}$  reduction at  $d = 20 \text{ mm}$  (see figure 8).

One interesting property of multi-element transducers that we also wanted to demonstrate is their ability to reduce the total scanning time. Significant time saving can for example be achieved by letting the individual elements generate parts of the image (hereafter denoted as subimages), which after the scanning, are assembled into one complete image. This will require parallel processing of two or more

elements, and we therefore made a realistic experimental test by driving two elements using a dual-channel signal generator and one current sense amplifier for which the experiment layout represented as a two-element operation mode in figure 9. These elements were driven by the same pulse form, but with a predefined time delay making it possible to separate the scattering caused by the individual elements when the digitized sampled time series were processed.

For our experimental test, two elements with aperture size B (with a center-to-center distance of 5 mm, defining the pitch) were scanned with steps of  $75 \mu\text{m}$  as before, yielding the two subimages shown in figure 12(e) after separating the scattering from the individual elements. The two images, each covering a size of  $6 \times 15 \text{ mm}^2$ , have some overlap which is indicated by the dash boxes with size  $1 \times 15 \text{ mm}^2$ . From the common color map used in the figures, we see a significant difference in the signal strength between the two elements. This difference, which is consistent with the variation previously shown in figure 5, needs to be compensated for prior to assembling the two images into one. For our transducer elements, the overall shapes of the frequency responses were found to vary much less than the signal amplitude (see figure 5 and table 1), and a fairly good compensation can therefore be obtained by just multiplying the intensities with a constant. This is illustrated in figure 12(f) where the intensities in the upper figure 12(e) have been scaled by a factor 1.45 before assembling the subimages into figure 12(f). For the assembled image, the overlapping regions have been removed yielding a final image size of  $11 \times 15 \text{ mm}^2$ . It should be emphasized that the computational time required for the image assembly steps in our prototype will normally be much less than the additional data acquisition scanning time. In fact, the sub-imaging method using two apertures investigated here, will reduce the total imaging time by almost a factor of two.

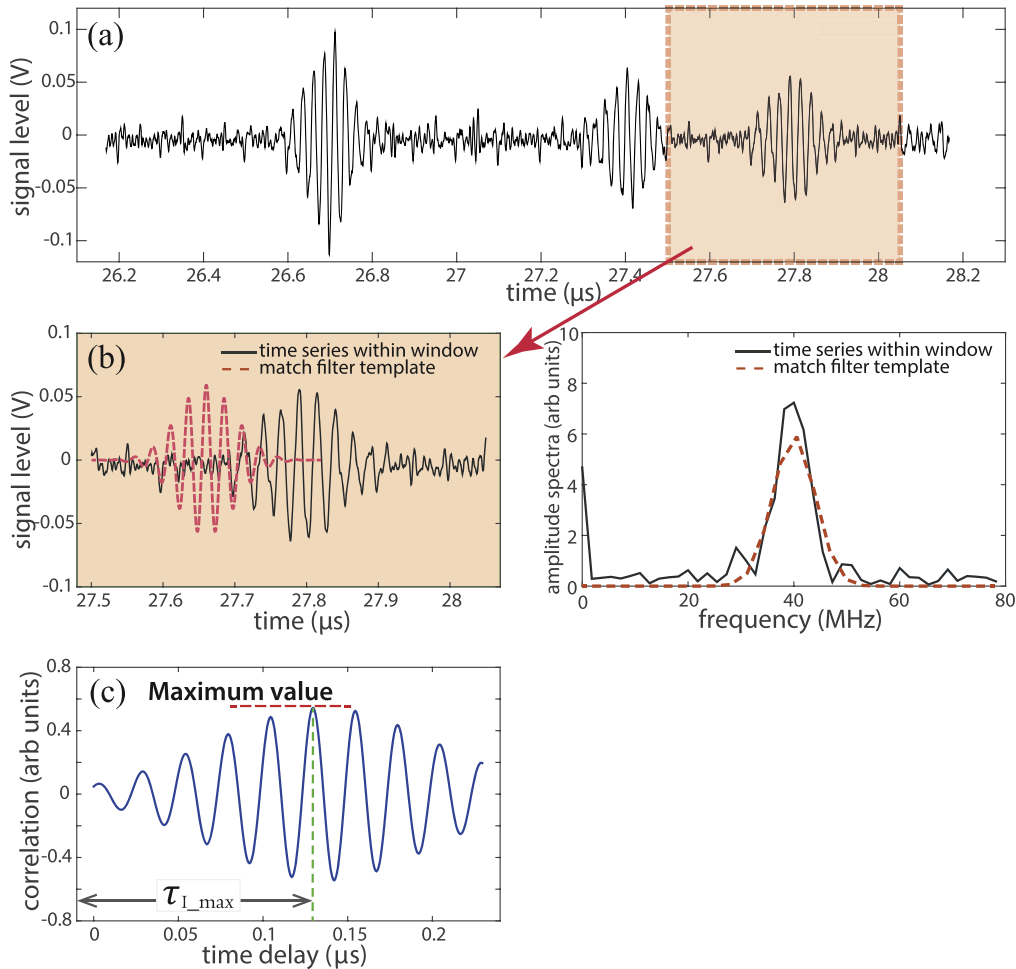


**Figure 11.** Examples of match filter processing. (a) The sample of acoustic response signals of received multi-echo waves in the water at single position, (b) the signal time series within the window and the template signal with frequency spectrum compared at right side and (c) convolution result which contains a magnitude of maximum amplitude correlation and its time delay.

#### 4.5. Multi-layer medium C-scan imaging

As a final test of our prototype, we wanted to image our PCB test specimen when it was placed inside a layered structure, thereby simulating a composited-material wave medium. The layered structure was comprised of a glass plate (thickness 1 mm) surrounded by distilled water, and our PCB test object. This is illustrated in the inset image of figure 9. The multi-layered wave medium is expected to induce more complex wave features, with multiple reflections caused by discontinuous acoustic material impedance (e.g. inside the glass plate), which make echoes on the receiver side more complicated to interpret. However, for the dimensions used in the experiment, the first echoes the PCB's copper side that we wanted to image could still be distinguished from the other reflections by applying a time-domain window. As before, a single element aperture of type B (see stand-alone mode operation) was scanned along the  $xy$  plane with a  $75 \mu\text{m}$  step length to generate the C-scan image shown in figure 13(a). From the image we notice that the smallest circular structure was almost invisible, and that the image contained more noise than the previous ones. According to match filter algorithm (figure 11), a signal delay time is also obtained from the

convolution. Figure 13(b) shows another style result created from time delay of maximum correlated amplitude, e.g.  $\tau_{I\_max}$  in figure 11(c), versus 2D location plot. From the figure, smallest circle can be noticed (pointed by arrow). Mapping of both results (intensity and delay) can help in structure identification. The effect induced by the glass plate on the acoustic beam was also measured using a needle hydrophone at  $d = 20$ , both with and without the glass plate inserted (placed around 17 mm from the transducer surface). From these measurements, a marginal change in 6 dB beamwidth from 0.78 to 0.85 mm (with inserted glass plate) was estimated.

## 5. Summary and conclusion

In the current work we have presented an adhesive-free method for making dual-layer polymer transducers with individual electrical connections to each element in a transducer array configuration. A number of prototypes were made, characterized by experimental and numerical means, and tested experimentally as imaging transducers in a water tank. Transducer elements with three different sizes were

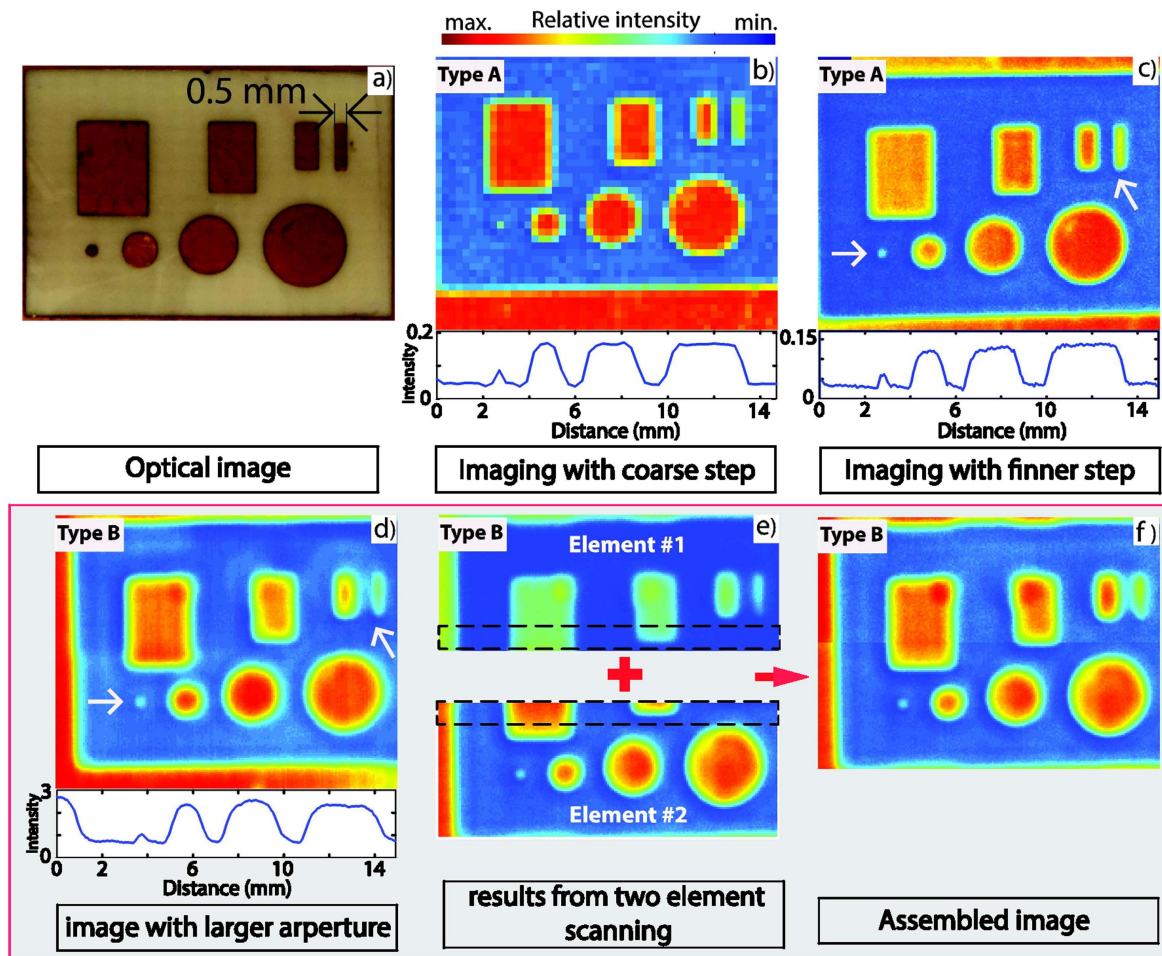


**Figure 12.** Results for the structural-scanned image experiments. (a) Optical image of the under-test PCB with copper 2D structures. The measured width of a smallest rectangular is around 0.5 mm. The resulting images created by scanning of (b) single element of type A at  $d = 10$  mm with scan step  $300 \mu\text{m}$  and (c) with scan step  $75 \mu\text{m}$ . The image scanned by larger aperture size; type B, at  $d = 20$  mm with scan step  $75 \mu\text{m}$  is (d). Results of dual-element scan test by scanning of type B elements at  $d = 20$  mm with scan step  $75 \mu\text{m}$  are (e) scan images from each individual operated element and (f) their assembled image.

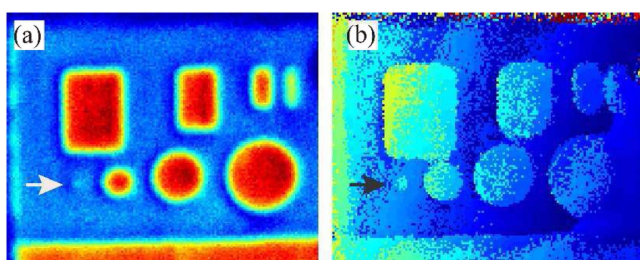


**Figure 13.** Demonstration of subsurface image scanning capability by operating element of type B in stand-alone mode scan. (a) The result shows C-scan image of the test PCB in composited medium depicted by inset image in figure 9. The  $d$  and a distance from the transducer to glass plate are 20 mm and 17 mm, respectively and (b) signal delay time versus 2D location plot.

produced and connected using a proposed via method involving two electrode deposition methods (sputtering and electroplating), chemical etching, and mechanical drilling of through-holes. Pins for electrical connection to the backside unit were inserted in these holes and filled with conductive epoxy, which in combination with thick metal pads, yielded a

short and uniform signal path length with improved connection robustness.

The polarized transducer elements made by our approach showed some variation in amplitude from element to element, but yielded a smaller variation in the shape of the frequency response. This gave a relatively reproducible center frequency around 42 MHz and a quite broad and constant bandwidth around 25 MHz, which is about 59% of the center frequency. It is also of interest to compare these numbers to other transducer with comparable materials and frequencies reported in [14, 28]. Here a 40 MHz focused transducer with conductive epoxy as the backing material in [14] yielded a 58% bandwidth whereas in [28], transducers with aluminum backing show 75% (in average). The transducer bandwidth is known to be influenced by a number of factors like for instance, backing materials [22], loading conditions and electrode thicknesses, which all can be plausible reasons for the obtained differences. It is also believed that the characterization instruments to some extent, will influence the measured bandwidths. Our current amplifier for example, has a specified upper bandwidth of 80 MHz for the used

amplification setting, but this frequency is known to be slightly dependent on the transducer capacitance. Higher capacitive loads will therefore give a lower cut-off frequency or less bandwidth since the upper  $-6$  dB edge is moving downward. It is likely that this effect is contributing to the frequency downshift observed for the largest apertures in figure 5.

It is also important to notice that the experimental investigation has shown that both the applied poling procedure and the following temperature treatment, are crucial steps for obtaining films with high signal amplitudes. It is therefore likely that spatial variation induced by these steps can explain the observed variation in signal amplitudes between elements. Estimated parameters like the center frequency and bandwidth on the other hand, are mainly determined by the ultrasonic wave field caused by the film thickness and the mechanical properties of P(VDF-TrFE) and the surrounding materials, and less correlated to the poling and annealing conditions. This is due to the relative low piezoelectric coupling coefficient for P(VDF-TrFE) typically ranging from 0.1 to 0.2. This will also be consistent with the experimental findings showing a much smaller variation in bandwidth parameters among transducer elements with the same aperture size.

Analytical estimates for the  $-6$  dB beamwidth at different distances (beyond the near-field region) obtained good match with the measured ones for all apertures. The measured acoustic field radiation from the transducer elements also resulted in a relatively symmetric field distribution for all aperture sizes. Our proposed transducer assembly method therefore looks promising with respect to future production of reliable and size-effective multilayer HF ultrasonic transducer arrays.

The experimental tests performed in a water scanning tank also suggest that the propose-built multi-element transducer has a significant potential for imaging, and for reducing the total inspection time by firing multiple elements simultaneously. The image tests showed that a structure diameter of at least 0.5 mm could be detected by both elements of type A and B. Experimental tests done with two element of type B with simultaneous overlapping imaging, also gave significant reduction in the scanning time. A generalization of this method to multi-element scanning could therefore give superior performance in term of for example, object identification at much faster scanning time. Moreover, the transducer prototype was also able to image structures underneath a solid layer (glass). This type of imaging is expected to be very challenging for a focused transducer due to the bending of the acoustic rays at the water-glass interfaces. In summary, we therefore believe that a further industrialization of the proposed dual-layer transducer array will have potential for application within many fields, especially when HFs and low cost are important issues.

## Acknowledgments

This work was supported by The Research Council of Norway through the project 'Subsea sensors'. The publication

charges for this article have been funded by a grant from the publication fund of UiT The Arctic University of Norway.

## ORCID iDs

Adit Decharat  <https://orcid.org/0000-0002-9545-6646>

## References

- [1] Goertz D E, Cherin E, Needles A, Karshafian R, Brown A S, Burns P N and Foster F S 2005 High frequency nonlinear B-scan imaging of microbubble contrast agents *IEEE Trans. Ultrason. Ferroelectr. Freq. Control* **52** 65–79
- [2] Baddour R E, Sherar M, Hunt J, Czarnota G and Kolios M C 2005 High-frequency ultrasound scattering from microspheres and single cells *J. Acoust. Soc. Am.* **117** 934–43
- [3] Foster F S, Harasiewicz K A and Sherar M D 2000 A history of medical and biological imaging with polyvinylidene fluoride (PVDF) transducers *IEEE Trans. Ultrason. Ferroelectr. Freq. Control* **47** 1363–71
- [4] Kimura K and Ohigashi H 1987 Generation of very high-frequency ultrasonic waves using thin films of vinylidene fluoride-trifluoroethylene copolymer *J. Appl. Phys.* **61** 4749–54
- [5] Wagle S, Decharat A, Bodö P and Melandsø F 2013 Ultrasonic properties of all-printed piezoelectric polymer transducers *Appl. Phys. Lett.* **103** 262902
- [6] Li M, Katsouras I, Piliago C, Glasser G, Lieberwirth I, Blom P W and de Leeuw D M 2013 Controlling the microstructure of poly (vinylidene-fluoride)(PVDF) thin films for microelectronics *J. Mater. Chem. C* **1** 7695–702
- [7] Brown L, Carlson R and Sempsrott J 1997 Spin-cast P (VDF-TrFE) films for high performance medical ultrasound transducers *Proc., 1997 IEEE Ultrasonics Symp., 1997 (IEEE)* pp 1725–7
- [8] Ramadan K S, Sameoto D and Evoy S 2014 A review of piezoelectric polymers as functional materials for electromechanical transducers *Smart Mater. Struct.* **23** 033001
- [9] Lukacs M, Sayer M, Lockwood G and Foster S 1999 Laser micromachined high frequency ultrasonic arrays *Proc. 1999 IEEE Ultrasonics Symp., 1999 (IEEE)* pp 1209–12
- [10] Pang G, Sayer M, Lockwood G R and Watt M 2006 Fabrication of PZT sol gel composite ultrasonic transducers using batch fabrication micromolding *IEEE Trans. Ultrason. Ferroelectr. Freq. Control* **53** 1679–84
- [11] Zhou Q, Wu D, Liu C, Zhu B, Djuth F and Shung K K 2010 Micro-machined high-frequency (80 MHz) PZT thick film linear arrays *IEEE Trans. Ultrason. Ferroelectr. Freq. Control* **57** 2213–20
- [12] Capineri L and Mazzoni M 2010 Laser pulses characterization with pyroelectric sensors *Laser Pulse Phenomena and Applications* (Rijeka: Intech) ch 9 (<https://doi.org/10.5772/13292>)
- [13] Bellan F, Bulletti A, Capineri L, Masotti L, Yarlioglu G G, Degertekin F L, Khuri-Yakub B, Guasti F and Rosi E 2005 A new design and manufacturing process for embedded Lamb waves interdigital transducers based on piezopolymer film *Sensors Actuators A* **123** 379–87
- [14] Turnbull D H, Starkoski B G, Harasiewicz K A, Semple J L, From L, Gupta A K, Sauder D N and Foster F S 1995 A 40–100 MHz B-scan ultrasound backscatter microscope for skin imaging *Ultrasound Med. Biol.* **21** 79–88

- [15] Sun L, Richard W D, Cannata J M, Feng C C, Johnson J A, Yen J T and Shung K K 2007 A high-frame rate high-frequency ultrasonic system for cardiac imaging in mice *IEEE Trans. Ultrason. Ferroelectr. Freq. Control* **54** 1648–55
- [16] Xie Q, Tao J, Wang Y, Geng J and Cheng S 2014 Use of ultrasonic array method for positioning multiple partial discharge sources in transformer oil *Rev. Sci. Instrum.* **85** 084705
- [17] Decharat A, Wagle S and Melandso F 2013 Evaluation of the acoustical properties of adhesive-free dual layer piezoelectric PVDF copolymer transducer *2013 Joint IEEE European Frequency and Time Forum and Int. Frequency Control Symp. (EFTF/IFC)* pp 266–9
- [18] Weerasekera R, Pamunuwa D, Zheng L-R and Tenhunen H 2009 Two-dimensional and three-dimensional integration of heterogeneous electronic systems under cost, performance, and technological constraints *IEEE Trans. Comput.-Aided Des. Integr. Circuits Syst.* **28** 1237–50
- [19] Zhang Q, Lewin P A and Bloomfield P E 1997 PVDF transducers—a performance comparison of single-layer and multilayer structures *IEEE Trans. Ultrason. Ferroelectr. Freq. Control* **44** 1148–56
- [20] Lilliehorn T, Blom T, Simu U, Johansson S, Nilsson M and Almqvist M 2005 Multilayer piezoelectric copolymer transducers *2005 IEEE Ultrasonics Symp. (IEEE)* pp 1618–20
- [21] Nakazawa M, Tabaru M, Nakamura K, Ueha S and Maezawa A 2007 Multilayered transducers using polyurea film *Japan. J. Appl. Phys.* **46** 4466
- [22] Sherar M and Foster F 1989 The design and fabrication of high frequency poly (vinylidene fluoride) transducers *Ultrason. Imaging* **11** 75–94
- [23] Edqvist E, Snis N and Johansson S 2007 Gentle dry etching of P (VDF-TrFE) multilayer micro actuator structures by use of an inductive coupled plasma *J. Micromech. Microeng.* **18** 015007
- [24] Choi S T, Kwon J O and Bauer F 2013 Multilayered relaxor ferroelectric polymer actuators for low-voltage operation fabricated with an adhesion-mediated film transfer technique *Sensors Actuators A* **203** 282–90
- [25] Decharat A, Wagle S, Jacobsen S and Melandsø F 2015 Using silver nano-particle ink in electrode fabrication of high frequency copolymer ultrasonic transducers: modeling and experimental investigation *Sensors* **15** 9210–27
- [26] <https://nde-ed.org/EducationResources/CommunityCollege/Ultrasonics/EquipmentTrans/beamsread.htm>
- [27] Motoyoshi M 2009 Through-silicon via (TSV) *Proc. IEEE* **97** 43–8
- [28] Robert M, Molingou G, Snook K, Cannata J and Shung K K 2004 Fabrication of focused poly (vinylidene fluoride-trifluoroethylene) P (VDF-TrFE) copolymer 40–50 MHz ultrasound transducers on curved surfaces *J. Appl. Phys.* **96** 252–6